Journal of Computational Physics **177,** 37–58 (2002)
doi:10.1006/jcph.2002.6998, available online at http://www.idealibrary.com on IDEAL®

An Essentially Nonoscillatory High-Order Padé-Type (ENO-Padé) Scheme

Zhiping Wang and George P. Huang[1]

Department of Mechanical Engineering, University of Kentucky, Lexington, Kentucky 40506-0108
E-mail: zpwang@engr.uky.edu and ghuang@engr.uky.edu

Received January 19, 2001; revised September 14, 2001

A new, essentially nonoscillatory high-order Padé-type (ENO-Padé) scheme has been developed by incorporating the ENO interpolation algorithm into the cell-centered Padé scheme. The scheme is designed to eliminate the nonphysical oscillatory behavior of the Padé scheme across discontinuities and to improve the performance of the ENO scheme in smooth regions. The main features of the ENO-Padé scheme are illustrated by the solution of the scalar transport equation, while the extension of the method to the solution of compressible flow equations is also demonstrated. A number of numerical test cases, including two scalar-transport problems and three compressible flows, are used to compare the performances of the ENO-Padé scheme against other available schemes, such as upwind-biased, Padé, and ENO schemes. The numerical results show that the ENO-Padé scheme is an excellent compromise of the available schemes for resolving profiles over flow discontinuities while maintaining accurate flow structures in smooth regions.

Key Words: high-order numerical techniques; finite-difference methods; compact differencing schemes; Padé scheme; ENO scheme.

1. INTRODUCTION

In the past decades, a number of high-order numerical schemes have been developed and applied to various flow simulations. Among these, Padé schemes [1], B-spline schemes [2, 3], FCT (flux-corrected transport) schemes [4], essentially nonoscillatory (ENO) schemes [5–8], weighted ENO (WENO) schemes [8–10], and high-order upwind-biased schemes [11, 12] are commonly used in CFD applications. In LES/DNS of complex turbulent flows, the use of nondissipative high-order numerical methods is becoming more and more popular. While for a steady-state Reynolds-average calculation the use of high-order numerical schemes can greatly reduce the number of grid points needed to achieve

[1] Fax: (859) 257-9258.

0021-9991/02 $35.00

a grid-independent solution, upwind-type high-order schemes have been found to produce significant numerical dissipative errors and hence are not suitable for LES/DNS calculations. A central-type high-order numerical scheme can prevent numerical dissipative errors from contaminating the physics of the flows and make numerical simulations more accurate and realistic.

Padé schemes, representing a family of compact high-order finite-difference schemes (derived in a very similar fashion to those obtained from Padé-approximants), were studied and used widely after Lele's paper in 1992 [1]. For example, a modified sixth-order Padé scheme was used by Mahesh *et al*. in their simulation of the interaction between a shock wave and a turbulent shear flow [13]. Likewise, Padé's formula was used to construct third- and fourth-order nonlinear numerical schemes in Deng and Maekawa's paper [14]. High-order Padé schemes using filtering techniques to smooth out spurious oscillations and numerical instabilities were also investigated in papers by Gaitonde and Visbal [15, 16].

Compared with explicit central-difference schemes, Padé schemes are implicit and hence global, such that the approximation to a derivative at one grid point involves the implicit solution of the field variables. Padé schemes give rise to a higher order of formal accuracy and better resolution characteristics for high-frequency waves than explicit central schemes do under the same stencil width [1]. Also, Padé schemes (except for boundary closure) are nondissipative schemes because of their inherent restriction of an assumed symmetry of the stencils and the corresponding coefficients. Unfortunately, like other central schemes, Padé schemes have been found to cause nonphysical oscillations when they are applied directly to discontinuous data. The nonphysical oscillations, which are known as the Gibbs phenomena in spectral methods, sometimes do not decay in magnitude, as the mesh is refined. In order to suppress the spurious oscillation and the nonlinear instability, Cockburn and Shu [17] developed nonlinearly stable compact schemes for shock calculations in 1994. They followed TVD (total variation diminishing) ideas to define a nonlinear limiter based on the local mean to avoid spurious oscillations while maintaining the formal accuracy of the scheme. However, spurious oscillations were still found in their numerical test problems for their fourth-order scheme. An extended and improved version of Cockburn and Shu's TVDM scheme can be found in Yee's recent paper [18].

On the other hand, ENO schemes show great promise for accurately treating flow discontinuities [5–8]. These schemes can be used to achieve a uniformly high-order accuracy yet maintain essentially nonoscillatory behavior for piecewise smooth functions by preventing the interpolation of the field values across the discontinuities as much as possible. This is done through a reconstruction or a flux evaluation procedure to allow the interpolating stencils to shift adaptively with the local smoothness of the function. For detailed information about ENO schemes, we refer readers to [8], which contains construction, analysis, and application of ENO and WENO schemes for hyperbolic conservation laws and related Hamilton–Jacobi equations. Although ENO schemes can be used for problems containing both discontinuities and complicated smooth flow structures, they might degenerate into upwind-type schemes in regions with moderately high, but still continuous, field gradients because the stencils chosen depend not only on the smoothness of the field values, but also on the flow direction (upwinding is the obvious choice to preserve the stability of the scheme). This may lead to some degrees of degradation for the numerical solutions in those regions due to the numerical dissipation of upwind-type schemes. Hence, the numerical solutions obtained with ENO schemes in smooth regions with moderately high field gradients are not as satisfactory as the solutions obtained with Padé schemes. One way to

eliminate this disadvantage of ENO schemes is to construct a hybrid scheme in which the scheme is switched to a conventional compact scheme in smooth regions and to the ENO scheme near discontinuities. Such a hybrid compact-ENO scheme has been proposed and studied by Adams and Shariff in [19]. A shortcoming of this type of hybridization is that the numerical solution might experience nonsmooth transitions near the interfaces where the scheme switches type. Some spurious waves might be generated at these interfaces between different schemes, and these spurious waves would eventually propagate into the smooth regions, as reported in [19].

The main objective of this paper is to develop an essentially nonoscillatory Padé-type (ENO-Padé) scheme, which combines general ENO ideas into conventional Padé schemes such that the nonphysical oscillation of Padé schemes near discontinuities can be eliminated (or at least be suppressed) while the high accuracy of Padé schemes in smooth regions can be maintained throughout. So the proposed ENO-Padé scheme is actually a compromise between Padé schemes and ENO schemes. In this paper, Section 2 illustrates the essential steps to construct high-order ENO-Padé schemes for scalar equations. In Section 3, the extension of the ENO-Padé scheme to compressible Euler equations of gas dynamics is discussed. Some numerical test cases are presented and discussed in Section 4. Finally, concluding remarks are provided in Section 5.

2. ENO-PADÉ SCHEME

The proposed numerical scheme is illustrated using the solution of the following 1-D scalar convection equation as an example.

$$\frac{\partial \phi}{\partial t} + \frac{\partial f(\phi)}{\partial x} = 0, \quad \text{with } f \equiv u\phi, \tag{1}$$

where u is the convecting velocity and ϕ is any scalar to be convected.

2.1. Padé Formula

Consider a uniform mesh arrangement with $x_i = ih, i = \frac{1}{2}, \frac{3}{2}, \ldots, N + \frac{1}{2}$ (nodal points are $i = 1, 2, \ldots, N$, here). We use a cell-centered Padé formula [1] to approximate the first spatial derivative, $f' = \partial f/\partial x$, in Eq. (1) as

$$\alpha f'_{i-1} + f'_i + \alpha f'_{i+1} = b\frac{f_{i+3/2} - f_{i-3/2}}{3h} + a\frac{f_{i+1/2} - f_{i-1/2}}{h}. \tag{2}$$

In the above implicit scheme, the nodes on which the first derivatives are calculated are staggered by a half-cell $(h/2)$ distance from the cell interfaces on which the field values are prescribed. This approximation arises naturally from a finite-volume discretization of conservation laws. Because the explicit part of Eq. (2) contains the field values at cell interfaces, an accurate interpolating scheme is needed to evaluate those interfacial values. We discuss this interpolating scheme in Section 2.2.

In Eq. (2), α, b, and a are Padé coefficients and can be determined by matching the Taylor series to different degrees of accuracy such that a family of numerical schemes can be obtained. The detailed general expressions for the coefficients and the corresponding truncation errors can be found in Appendix B of Ref. [1] and are not repeated here.

Throughout this paper, a sixth-order, cell-centered Padé scheme is used for the interior nodal points ($i = 3, \ldots, N-2$), with its coefficients given as

$$\alpha = \frac{9}{62}, \quad a = \frac{63}{62}, \quad b = \frac{17}{62}. \tag{3}$$

The corresponding truncation error of this scheme is $(61/277760)h^6(\partial^7 f/\partial x^7)$.

For the nodal points near boundaries ($i = 1, 2$ and $i = N-1, N$), the above scheme (2) combined with coefficients (3) can be applied directly to a periodic boundary without any modification, while special treatments are needed at a nonperiodic direction. (It should be noted that the cell edges $i = \frac{1}{2}$ and $i = N + \frac{1}{2}$ are the actual boundaries in our mesh arrangement.)

For a nonperiodic boundary, a one-sided scheme with reduced order of accuracy is applied to $i = 1$ and $i = N$, i.e.,

$$f_1' + \alpha_1 f_2' = \frac{1}{h}\left(a_1 f_{1/2} + b_1 f_{3/2} + c_1 f_{5/2}\right), \tag{4}$$

$$\alpha_2 f_{N-1}' + f_N' = \frac{1}{h}\left(c_2 f_{N-3/2} + b_2 f_{N-1/2} + a_2 f_{N+1/2}\right), \tag{5}$$

where $\alpha_1 = -1, a_1 = -1, b_1 = 2, c_1 = -1, \alpha_2 = -1, a_2 = 1, b_2 = -2,$ and $c_2 = 1$. Both boundary schemes (4) and (5) are third-order accurate and the tridiagonal feature of the scheme (2) is also preserved.

For $i = 2$ and $i = N-1$, the same scheme as (2) can be used, but a modification of the coefficients for the scheme is needed to satisfy the global conservation law in a discrete form. Lele discussed this issue in detail for general compact schemes in Ref. [1] and Deng and MaeKawa [14] also gave a simple approach for their high-order nonlinear schemes to guarantee the global conservation requirement. Following their approaches, the modified coefficients for the near-boundary schemes ($i = 2$ and $i = N-1$) have been derived (see the appendix) and yields

$$\hat{\alpha} = \frac{55}{666}, \quad \hat{a} = \frac{118}{111}, \quad \hat{b} = \frac{34}{333}. \tag{6}$$

The resulting near-boundary schemes are fourth-order accurate and satisfy the global conservation requirement.

The Padé scheme (2) and the derived boundary schemes constitute a tridiagonal linear system that can be efficiently solved to get the approximate first spatial derivative at every nodal point.

It should be noted that although the above Padé formulae are presented for a uniformly arranged mesh, they can be easily extended to a nonuniform mesh by means of a general coordinate transformation.

2.2. ENO Interpolation

The right-hand-side of the Padé scheme (2) contains the field values at cell interfaces. As mentioned previously, this makes it necessary to use an accurate interpolating technique. There are a number of approximations available to perform the interpolation. In

this paper, a modified ENO interpolating scheme is used to achieve a high-order accuracy while maintaining the essentially nonoscillatory behavior. The ENO interpolation algorithm allows the interpolating stencils to shift adaptively according to the smoothness of the field values in the neighboring stencils such that the interpolation across discontinuities is avoided as much as possible. The moving-stencil strategy reduces, and sometimes suppresses, the nonphysical oscillation and the numerical instability occurring in the solution.

The interfacial value of $f_{i+1/2}$ $(i = 0, 1, 2, \ldots, N)$ can be obtained from

$$f_{i+1/2} = \frac{1}{2}\left(f^L_{i+1/2} + f^R_{i+1/2}\right) - \frac{1}{2}\frac{a_{i+1/2}}{\left|a_{i+1/2}\right|}\left(f^R_{i+1/2} - f^L_{i+1/2}\right), \tag{7}$$

where $f^L_{i+1/2}$ is the left-interfacial value obtained by ENO interpolation using the left stencil and $f^R_{i+1/2}$ is the right-interfacial value obtained by ENO interpolation using the right stencil. $a_{i+1/2}$ is the Roe speed at $x_{i+1/2}$, defined by $a_{i+1/2} = \frac{f_{i+1} - f_i}{\phi_{i+1} - \phi_i}$. Equation (7) is essentially an upwinding formula for the interfacial fluxes.

The left stencil covers the stencil point x_i and its neighboring points, while the right stencil includes the stencil point x_{i+1} and its neighboring points. The number of stencil points needed to approximate the interfacial value is determined by the order of accuracy of the scheme selected. For instance, an n-point stencil is needed if the scheme is nth-order accurate and the number of available left stencil groups for $f^L_{i+1/2}$ (or available right stencil groups for $f^R_{i+1/2}$) is also n. The available left stencil groups for $f^L_{i+1/2}$ include $(x_{i-n+1}, x_{i-n+2}, \ldots, x_i)$, $(x_{i-n+2}, x_{i-n+3}, \ldots, x_{i+1}), \ldots,$ and $(x_i, x_{i+1}, \ldots, x_{i+n-1})$, while the available right stencil groups for $f^R_{i+1/2}$ include $(x_{i-n+2}, x_{i-n+3}, \ldots, x_{i+1})$, $(x_{i-n+3}, x_{i-n+4}, \ldots, x_{i+2}), \ldots,$ and $(x_{i+1}, x_{i+2}, \ldots, x_{i+n})$. Among those available stencil groups, the smoothest one will be selected automatically by using an ENO algorithm. Once a group of the stencil points is selected, Newton polynomial interpolation can be used to obtain the interfacial fluxes: $f^L_{i+1/2}$ (or $f^R_{i+1/2}$).

For example, in order to achieve rth order accuracy for $f^L_{i+1/2}$, an $(r-1)$th degree polynomial $P^{(r-1)}_{i+1/2}(x)$ at interval $[x_{i-1/2}, x_{i+1/2}]$ can be constructed by performing Newton interpolation at the left stencil $\{x_{k^{(r-1)}_{min}}, x_{k^{(r-1)}_{min}+1}, \ldots, x_{k^{(r-1)}_{min}+r-1}\}$ as

$$P^{(r-1)}_{i+1/2}(x) = f\left[x_{k^{(r-1)}_{min}}\right] + \sum_{l=1}^{r-1}\left(f\left[x_{k^{(r-1)}_{min}}, \ldots, x_{k^{(r-1)}_{min}+l}\right]\prod_{j=k^{(r-1)}_{min}}^{k^{(r-1)}_{min}+l-1}(x - x_j)\right), \tag{8}$$

where $f[., \ldots, .]$ are the standard Newton divided differences and are recursively defined as

$$f[x_1, x_2, \ldots, x_{k+1}] = \frac{f[x_2, \ldots, x_{k+1}] - f[x_1, \ldots, x_k]}{x_{k+1} - x_1}, \tag{9}$$

with $f[x_i] = f(x_i)$. $x_{k^{(r-1)}_{min}}$ is the left-most stencil point in the left stencil.

The ENO algorithm that chooses the stencil group used for $f^L_{i+1/2}$ (or $f^R_{i+1/2}$) actually selects only the left-most stencil point, $x_{k^{(r-1)}_{min}}$. As long as the left-most stencil point is determined, the whole stencil group is selected. The left-most stencil point, $x_{k^{(r-1)}_{min}}$, in the left stencil can be selected by using the following algorithm.

ALGORITHM 1.

Begin
  $k_{min}^{(0)} := i$;
  For $l = 1$ **to** $l = r - 1$, **do**
    $a^{(l)} := f[x_{k_{min}^{(l-1)}}, \ldots, x_{k_{min}^{(l-1)}+l}]$;
    $b^{(l)} := f[x_{k_{min}^{(l-1)}-1}, \ldots, x_{k_{min}^{(l-1)}+l-1}]$;
    If $x_{k_{min}^{(l-1)}} > x_{k_{min}^{pref}}$, **then do**
      If $\beta|a^{(l)}| \geq |b^{(l)}|$, **then do**
        $k_{min}^{(l)} := k_{min}^{(l-1)} - 1$;
      Otherwise, do
        $k_{min}^{(l)} := k_{min}^{(l-1)}$;
      End If
    Otherwise, do
      If $|a^{(l)}| > \beta|b^{(l)}|$, **then do**
        $k_{min}^{(l)} := k_{min}^{(l-1)} - 1$;
      Otherwise, do
        $k_{min}^{(l)} := k_{min}^{(l-1)}$;
      End If
    End If
  End For
End

Here, the biasing strategy proposed by Fatemi *et al*. [20] and Shu [21] is employed to avoid the unnecessary moving of stencils due to small fluctuations in the solution and its derivatives during iterations. An initial preferred stencil group $\{x_{k_{min}^{pref}}, x_{k_{min}^{pref}+1}, \ldots, x_{k_{min}^{pref}+r-1}\}$, which might be central or one-point upwind-biased depending on whether the stencil group contains an even or an odd number of nodal points, is first identified for $f_{i+1/2}^{L}$. The variable $\beta(\geq 1)$ is an adjustable biasing parameter to allow the selected stencil to stay as close as possible to the preferred stencil. Unless an alternative candidate group is a factor of β better in smoothness than the preferred stencil, the preferred stencil remains the same. Otherwise, the alternative candidate will become the new preferred stencil group. The greater the value of β is, the closer to the original preferred stencil group the interpolation becomes. A value of $\beta = 1.5$ is recommended in the present work.

Similarly, $f_{i+1/2}^{R}$ can be obtained by replacing $k_{min}^{(0)} := i$ in the second line of the above algorithm with $k_{min}^{(0)} := i + 1$ and following the same procedure.

2.3. Analysis of ENO-Padé Scheme

The proposed ENO-Padé scheme has two major steps: ENO interpolation is performed first to get all the interfacial fluxes, and a cell-centered Padé scheme is then applied to compute the first derivatives at all nodal points.

The ENO-Padé scheme is highly nonlinear because of its adaptive selection of stencil in the ENO interpolation step and hence standard linear stability analysis is not appropriate for the ENO-Padé scheme. However, the ENO-Padé scheme, like other ENO-type schemes, shows excellent numerical stability in our test problems. As pointed out in [5], once oscillations and instability appear on the level of the highest derivative and are ready to propagate to the function itself, the adaptive selection of a stencil in an ENO procedure reacts by

changing the orientation of the stencil and thus avoids the buildup of instability. This is the reason that ENO-type schemes are usually highly stable.

It is also obvious that the overall formal accuracy of the ENO-Padé scheme is determined by both the order of accuracy of the Padé formula and that of the ENO interpolation. Suppose the interfacial flux $f_{i+1/2}$ is interpolated to rth-order accuracy, i.e.,

$$f_{i+1/2} = f\left(x_{i+1/2}\right) + d\left(x_{i+1/2}\right)h^r + O(h^{r+1}). \tag{10}$$

Substituting (10) into (2) with coefficients (3) and performing a Taylor series expansion on both sides of (2) at x_i, we can get

$$f_i' = \left(\frac{\partial f}{\partial x}\right)_i + \frac{61}{277760}\left(\frac{\partial^7 f}{\partial x^7}\right)_i h^6 + \left[b\frac{d\left(x_{i+3/2}\right) - d\left(x_{i-3/2}\right)}{3h} + a\frac{d\left(x_{i+1/2}\right) - d\left(x_{i-1/2}\right)}{h}\right]h^r + O(h^8, h^{r+1}). \tag{11}$$

So the ENO-Padé scheme is sixth-order accurate if $r \geq 6$ and $d(x)$ is Lipschitz continuous. If $r < 6$ and $d(x)$ is Lipschitz continuous, the scheme is only rth-order accurate in the sense of overall formal accuracy. When $d(x)$ fails to be Lipschitz continuous at some special points, the local truncation error of the ENO-Padé scheme might be one order lower.

Based on the above analysis of the formal accuracy, a sixth-order ENO interpolation scheme is applied at every interior cell interface for the values of $f^L_{i+1/2}$ and $f^R_{i+1/2}$ to make the proposed ENO-Padé scheme sixth-order accurate at interior points. Similar to the boundary closure of the cell-centered Padé scheme discussed earlier, the same ENO interpolation scheme with a reduced order of accuracy is applied for near-boundary cell interfaces if the boundary is nonperiodic.

2.4. Time Discretization

One of our main objectives in developing the ENO-Padé scheme is to use the developed and validated scheme in the simulation of complex wall-bounded turbulent flows, which are of major interest to many researchers and engineers. For such wall-bounded flows, explicit time-integration methods are usually a poor choice due to the fact that the very fine mesh arrangement near the wall puts a far too stringent time-step size constraint on simulation. An implicit method does not have this constraint and a larger time-step size can be employed. Therefore, although the explicit time-integration methods like high-order TVD-type Runge–Kutta methods presented in [6] can be used for time discretization, we are more interested in coupling the ENO-Padé scheme with an implicit method.

In this paper, a second-order fully implicit scheme is used for the temporal discretization of Eq. (1),

$$\frac{3\phi^{n+1} - 4\phi^n + \phi^{n-1}}{2\Delta t} + \frac{\partial f(\phi^{n+1})}{\partial x} = 0, \tag{12}$$

and a deferred iterative solution algorithm is employed to obtain the solution of ϕ^{n+1} by substituting

$$(\phi^{n+1})^{m+1} = (\phi^{n+1})^m + (\Delta\phi)^m \tag{13}$$

into (12), where the superscript m stands for the inner iteration level. The final equation is

$$\frac{3}{2}\frac{(\Delta\phi)^m}{\Delta t}+\frac{\partial u(\Delta\phi)^m}{\partial x}=\frac{(\phi^n-\phi^{n-1})}{2\Delta t}-\frac{3}{2}\frac{((\phi^{n+1})^m-\phi^n)}{\Delta t}-\frac{\partial f((\phi^{n+1})^m)}{\partial x}. \quad (14)$$

The right-hand-side of Eq. (14) is explicit and the ENO-Padé scheme can be implemented in a straightforward manner to discretize the spatial derivative term. To ensure stability of the iterative procedure, a first-order upwind scheme is used to discretize the spatial derivative in the left-hand-side and the solution is obtained by performing inner iterations to drive the right-hand-side of (14) to zero. The deferred iterative algorithm is strongly stable, and as long as the right-hand-side of Eq. (14) is zero, the ENO-Padé solution for ϕ^{n+1} is obtained. Because an inner iterative procedure is performed at every time step, this method is fully implicit.

3. EXTENSION TO EULER EQUATIONS

To illustrate the extension of the ENO-Padé scheme to compressible flow equations, the following 1-D Euler equations are solved numerically. However, the extension of the current approach to multidimensional cases can be achieved in a straightforward, dimension-by-dimension fashion.

The 1-D Euler equations can be written as

$$\frac{\partial Q}{\partial t}+\frac{\partial F}{\partial x}=0, \quad (15)$$

where

$$Q=\begin{pmatrix}\rho\\ \rho U\\ \rho E\end{pmatrix},\quad F=\begin{pmatrix}\rho U\\ \rho U^2+P\\ \rho U(E+P/\rho)\end{pmatrix}.$$

For a perfect gas,

$$P=\rho(\gamma-1)\left(E-\frac{1}{2}U^2\right), \quad (16)$$

$$E=c_vT+\frac{1}{2}U^2. \quad (17)$$

Here, ρ, U, P, T, and E are density, velocity, pressure, temperature, and total energy, respectively. c_v is the specific heat at constant volume and γ is the specific heat ratio.

The second-order, fully implicit time discretization and the deferred iterative solution procedure discussed in the previous section are used to solve the Euler equations. The spatial derivative term, $\partial F/\partial x$, can be evaluated by the ENO-Padé scheme in a componentwise fashion, with the interfacial fluxes, $F_{i+1/2}$, being calculated by Roe's approximate Riemann solver [22],

$$F_{i+1/2}=\frac{1}{2}\left(F\left(Q^R_{i+1/2}\right)+F\left(Q^L_{i+1/2}\right)\right)-\frac{1}{2}\left|A_{i+1/2}\right|\left(Q^R_{i+1/2}-Q^L_{i+1/2}\right), \quad (18)$$

where the superscripts L and R stand for the left-interfacial value and the right-interfacial value. Matrix A ($\equiv\partial F/\partial Q$) is the Jacobian matrix and can be diagonalized by its similarity matrix R,

$$A=\frac{\partial F}{\partial Q}=R^{-1}\Lambda R, \quad (19)$$

with

$$\Lambda = \begin{pmatrix} U & 0 & 0 \\ 0 & U+c & 0 \\ 0 & 0 & U-c \end{pmatrix}, \tag{20a}$$

$$R = \begin{pmatrix} \frac{1}{2}(\gamma-1)U^2 - c^2 & (1-\gamma)U & (\gamma-1) \\ \frac{1}{2}(\gamma-1)U^2 - cU & (1-\gamma)U + c & (\gamma-1) \\ \frac{1}{2}(\gamma-1)U^2 + cU & (1-\gamma)U - c & (\gamma-1) \end{pmatrix}, \tag{20b}$$

$$R^{-1} = \begin{pmatrix} -1/c^2 & 1/(2c^2) & 1/(2c^2) \\ -U/c^2 & (U+c)/(2c^2) & (U-c)/(2c^2) \\ -U^2/(2c^2) & \frac{U^2}{4c^2} + \frac{U}{2c} + \frac{1}{2(\gamma-1)} & \frac{U^2}{4c^2} - \frac{U}{2c} + \frac{1}{2(\gamma-1)} \end{pmatrix}, \tag{20c}$$

where U, $U+c$, and $U-c$ are the eigenvalues of the Jacobian matrix A and $c = \sqrt{\gamma p/\rho}$ is the speed of sound.

The ENO interpolation algorithm discussed in the previous section can be used to compute the components of $Q^R_{i+1/2}$ and $Q^L_{i+1/2}$ in Eq. (18) and $|A_{i+1/2}|$ in the same equation can be computed by

$$\left|A_{i+1/2}\right| = R^{-1}_{i+1/2} \cdot \begin{pmatrix} |U|_{i+1/2} & 0 & 0 \\ 0 & |U+c|_{i+1/2} & 0 \\ 0 & 0 & |U-c|_{i+1/2} \end{pmatrix} \cdot R_{i+1/2}. \tag{21}$$

Furthermore, in order to calculate the values of $R^{-1}_{i+1/2}$, $R_{i+1/2}$, and $|\Lambda|_{i+1/2}$, which are functions of $U_{i+1/2}$ and $c_{i+1/2}$, Roe average can be applied to calculate $U_{i+1/2}$ and $c_{i+1/2}$ by

$$\beta = \sqrt{\frac{\rho^R_{i+1/2}}{\rho^L_{i+1/2}}}, \tag{22a}$$

$$U_{i+1/2} = \frac{U^L_{i+1/2} + \beta U^R_{i+1/2}}{1+\beta}, \tag{22b}$$

$$H_{i+1/2} = \frac{H^L_{i+1/2} + \beta H^R_{i+1/2}}{1+\beta}, \quad \text{with } H \equiv E + \frac{P}{\rho}, \tag{22c}$$

$$c_{i+1/2} = \sqrt{(\gamma-1)\left(H_{i+1/2} - \frac{1}{2}U^2_{i+1/2}\right)}. \tag{22d}$$

The combination of approximate Riemann solver and Roe average is one simple way to evaluate the interfacial fluxes. Alternatively, we can also slightly modify Eq. (18) into

$$\begin{aligned} F_{i+1/2} &= F\left(Q^H_{i+1/2}\right) - \frac{1}{2}\left|A^H_{i+1/2}\right|\left(Q^R_{i+1/2} - Q^L_{i+1/2}\right) \\ &= F\left(Q^H_{i+1/2}\right) - \frac{1}{2}R^{-1,H}_{i+1/2}\left|\Lambda^H_{i+1/2}\right|R^H_{i+1/2}\left(Q^R_{i+1/2} - Q^L_{i+1/2}\right) \\ &= F\left(Z^H_{i+1/2}V^H_{i+1/2}\right) - \frac{1}{2}R^{-1,H}_{i+1/2}\left|\Lambda^H_{i+1/2}\right|R^H_{i+1/2}Z^H_{i+1/2}\left(V^R_{i+1/2} - V^L_{i+1/2}\right), \end{aligned} \tag{23}$$

where $V \equiv [\rho, u, p]^T$ is the vector of primitive variables and Z is the transformation matrix between the conservative variables (Q) and the primitive variables (V), with $Q = Z \cdot V$,

$$Z = \begin{pmatrix} 1 & 0 & 0 \\ 0 & \rho & 0 \\ \frac{1}{2}U^2 & 0 & \frac{1}{\gamma - 1} \end{pmatrix}. \tag{24}$$

$V^R_{i+1/2}$ and $V^L_{i+1/2}$ in Eq. (23) can be calculated by the ENO interpolation algorithm illustrated in the previous section. $V^H_{i+1/2}$ must be evaluated by using a high-order central scheme that is at least one order higher than the order of accuracy of the ENO interpolation scheme used in calculating $V^R_{i+1/2}$ and $V^L_{i+1/2}$. The values of $R^{-1,H}_{i+1/2}$, $R^H_{i+1/2}$, $\Lambda^H_{i+1/2}$, $Z^H_{i+1/2}$, and $F(Z^H_{i+1/2}V^H_{i+1/2})$ can be evaluated once $V^H_{i+1/2}$ is defined. Note that the order of accuracy of (23) is still determined by the order of accuracy of the ENO interpolation scheme used—sixth order for interior points throughout this paper.

Although the second method (Eq. (23)) does not make use of the Roe average, we find that it is very robust and it works very well in our numerical test problems.

After the interfacial fluxes, $F_{i+1/2}$, have been evaluated, the cell-centered Padé scheme (2) is used to obtain the spatial derivative, $\partial F/\partial x$, as discussed in Section 2.

4. NUMERICAL TEST CASES

In the following numerical test problems, we compare the performance of the proposed sixth-order ENO-Padé scheme with three popular high-order numerical schemes: the fifth-order upwind-biased scheme [11, 12], the sixth-order Padé scheme proposed by Lele [1], and the sixth-order ENO-Roe scheme developed by Shu and Osher [7]. Detailed formulae and information about these three schemes can be found in [11], [1], and [7], respectively.

For every test problem in this section, all computations are performed with the second-order, fully implicit time-integration method, discussed in Section 2.4. The same computational domain, mesh arrangement, boundary conditions, and time-step size are used for all schemes.

4.1. Scalar Cases

The first scalar test case is the rotation of a Gaussian profile, given by

$$\phi(x, y) = \exp\left(-\frac{r^2}{2\sigma^2}\right), \tag{25}$$

with

$$r = \sqrt{(x - x_c)^2 + (y - y_c)^2},$$

where (x_c, y_c) is the central point of the profile and σ is a constant. We take $\sigma = 1$ in this case. The computational domain is set to $0 \le x \le 30$, $0 \le y \le 30$ and the initial central point of the Gaussian profile is located at (15, 22.5). The initial profile is shown in Fig. 1.

The governing equation for the motion of scalar ϕ in Cartesian coordinates is given by

$$\frac{\partial \phi}{\partial t} + \frac{\partial u\phi}{\partial x} + \frac{\partial v\phi}{\partial y} = 0, \tag{26}$$

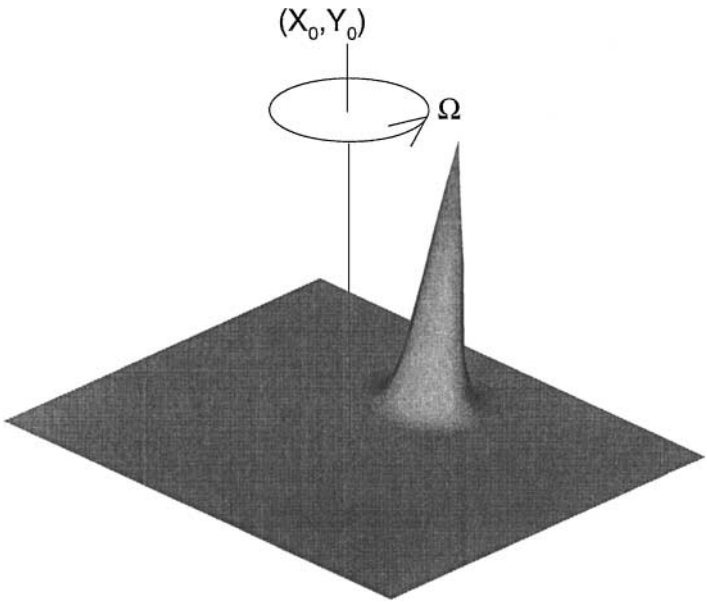

FIG. 1. Perspective view of the initial Gaussian profile.

where $u = -\Omega(y - y_0)$ and $v = \Omega(x - x_0)$. $\Omega(=2\pi/360)$ is the constant rotating angular velocity. (x_0, y_0) is the axis of the rotation and is set to (15, 15) in this case.

Since there is no physical diffusion imposed in the motion, the profile should keep its original shape unchanged during the rotation. This is obviously impossible for numerical solutions because all numerical schemes are subject to some degree of numerical error. As a result, the degree of the predicted shape distortion after one full rotation cycle will reflect the performance of the numerical schemes.

Figure 2 shows the comparison of the performance of the numerical schemes on a uniform mesh (40×40) with a time-step size of $\Delta t = 0.25$. This time-step size corresponds to a CFL

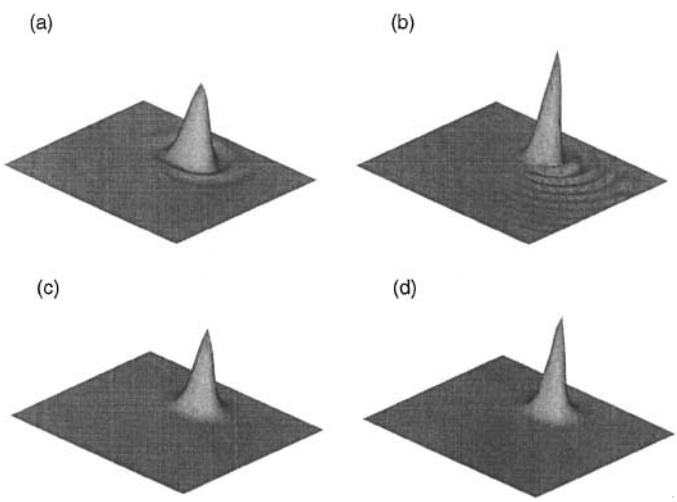

FIG. 2. Perspective view of the numerical results for the rotation of a Gaussian profile after one full cycle: (a) fifth-order upwind-biased scheme; (b) Pade scheme; (c) ENO-Roe scheme; (d) ENO-Pade scheme.

number of 0.087 and further reduction of the time-step size yields no perceptible impact on the numerical solution for all schemes.

From Fig. 2, it is clear that the Padé scheme is the most accurate one, but it shows slight spurious oscillations. The fifth-order upwind-biased scheme is strongly diffusive and displays some degrees of oscillation. The ENO-Roe scheme is basically nonoscillatory, but it is also very diffusive in this case. The proposed sixth-order ENO-Padé scheme not only presents a nonoscillatory behavior, it also shows a relatively accurate solution. Overall, the ENO-Padé scheme provides the best performance in this case.

Notice that the 40×40 mesh used here is deliberately designed to be coarse enough to distinguish the accuracy of various schemes. Further study shows that when the mesh is refined to 80×80, the oscillations in the Padé solution disappear and the Padé scheme predicts the best result. This is not surprising since the Gaussian profile resolved in this case is a smooth profile, and the Padé scheme gives the best performance in smooth regions. However, the spurious oscillations arising from applying the Padé scheme directly to discontinuous data cannot be eliminated or suppressed by simply performing a mesh refinement.

Figure 3 shows the error convergence rates with mesh refinement for different numerical schemes. The mesh size ranges from (20×20) to (160×160). To guarantee that the truncation error is really dominated by the spatial discretization, a sufficiently small time-step size of $\Delta t = 0.0125$, which corresponds to a CFL number of 0.0174 on the finest mesh, is used for all runs. Figure 3a shows the comparison of the L_2 norms, while the errors of the predicted peak value of the profile are shown in Fig. 3b. Since the numerical diffusion causes the profile to decay as it rotates, the error of the predicted peak value is actually an indicator of the numerical diffusion of the scheme. From Fig. 3a, it can be shown that the Padé, ENO-Padé, and ENO-Roe schemes converge approximately at sixth-order accuracy, and that the fifth-order upwind-biased scheme exhibits a fifth-order accuracy. Nonetheless, the Padé and ENO-Padé scheme show much smaller L_2 errors than the fifth-order upwind-biased scheme and ENO-Roe scheme do. For the ENO-Roe scheme, we also note that the well-known order-degeneracy phenomenon, reported by Rogerson and Meiburg [23] and Shu [21], appears when the mesh is refined to 160×160. Figure 3b shows that the Padé scheme presents the least numerical diffusion among all schemes, while the ENO-Padé scheme comes second. Their results show less numerical diffusion than the ENO-Roe scheme and the fifth-order upwind-biased scheme.

The second scalar test case is taken from Zalesak's paper in 1979 [4]. It involves the rotation of a cut-out cylinder with strong contact discontinuities in the profile. Figure 4 is a schematic representation of this problem. Initially, the scalar value inside the cut-out cylinder is 3.0, while it is 1.0 in other regions. The computational domain is set to $0 \le x \le 10, 0 \le y \le 10$ and $(x_0, y_0) = (5, 5)$ is the axis of the rotation. The center of the cut-out cylinder is located in $(x_c, y_c) = (5, 7.5)$ initially and the radius is 1.5. A perspective view of the initial profile is shown in Fig. 5.

Again, the physical diffusion is switched off and the angular velocity, Ω, is set to $2\pi/360$, as in the first test case. All computations are carried out on a uniform mesh of 120×120 with a small time-step size of $\Delta t = 0.25$. The perspective views of the numerical results after one full cycle of rotation for different schemes are presented in Fig. 6. It can be seen that the proposed ENO-Padé scheme gives the best performance among all tested schemes. The Padé scheme gives rise to severe oscillatory behavior everywhere in the domain. The fifth-order upwind-biased scheme exhibits both excessive numerical diffusion and some degrees of oscillation. The ENO-Roe scheme shows a nonoscillatory performance, but its dissipation is relatively large compared to the ENO-Padé scheme. This can be more clearly

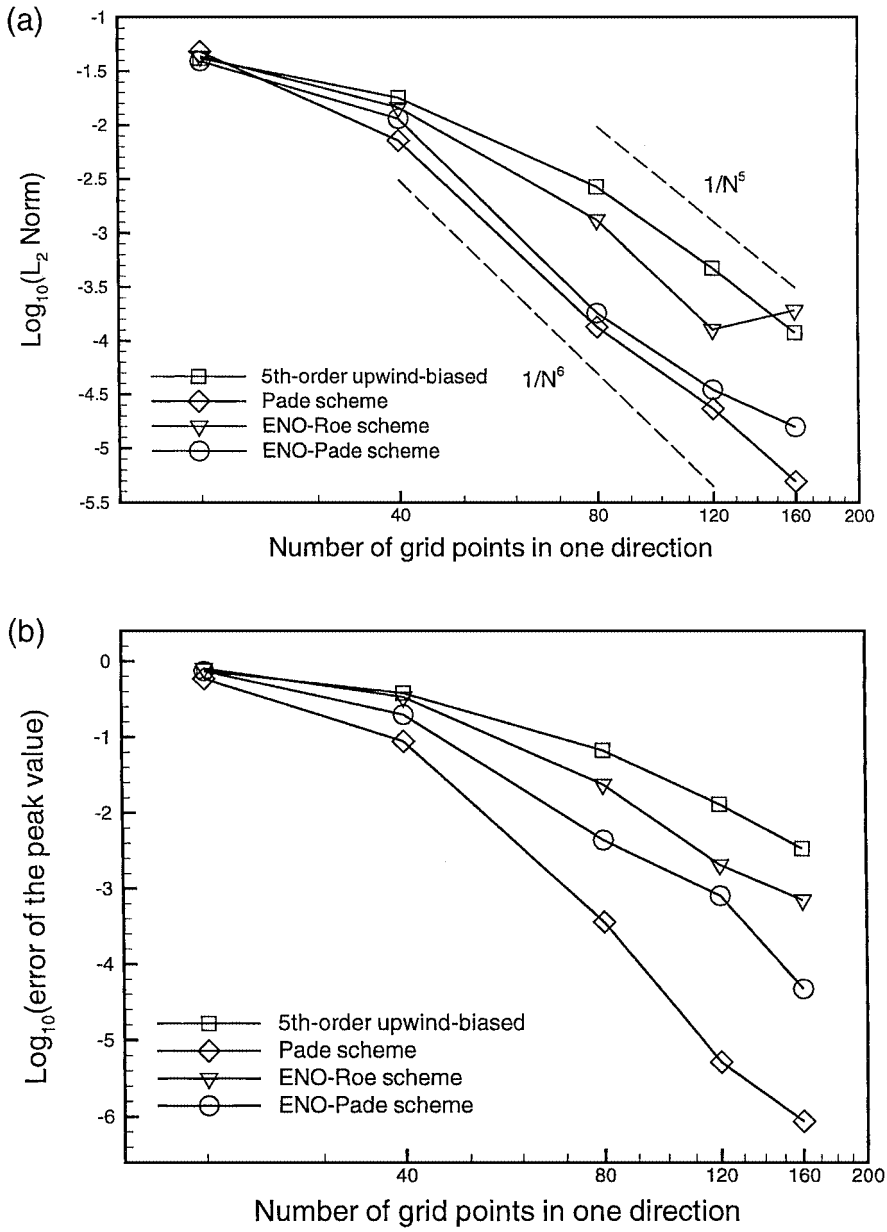

FIG. 3. The grid convergence study for different schemes: (a) L_2 norm; (b) error of the peak value.

seen from Fig. 7, which shows the comparison of the predicted profiles by the ENO-Roe scheme and the ENO-Padé scheme along the line $y = 7.5$. Overall, the ENO-Padé scheme not only shows a nonoscillatory behavior, it also gives rise to the best profile shape, as compared with the initial profile.

4.2. Compressible Flow Cases

The first test case in compressible flows is a 1-D gas dynamic problem with a moving Mach 3 shock interacting with the small disturbance in density [7]. The problem is governed

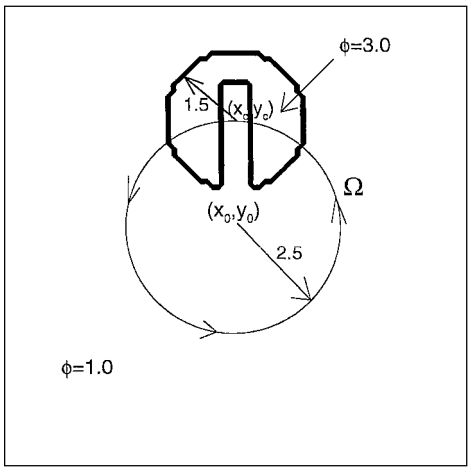

FIG. 4. Schematic representation of the cut-out cylinder rotation problem.

by 1-D Euler equations with the following initial conditions:

$$(\rho, u, p) = \begin{cases} (3.857143, 2.629369, 10.33333), & \text{if } x < -4; \\ (1 + 0.2 \sin 5x, 0, 1), & \text{otherwise.} \end{cases} \tag{27}$$

At $t = 0$, the Mach 3 shock is at location $x = -4$ and moves to the right into a state with sine waves in density. As the flow develops downstream, it will form a number of fine structures in the density profile of the postshock region. This problem is also regarded as a model problem for "shock/turbulence" interaction by some researchers and a linearized analysis can be found in [24], while numerical solutions have been presented in [7, 14, 19].

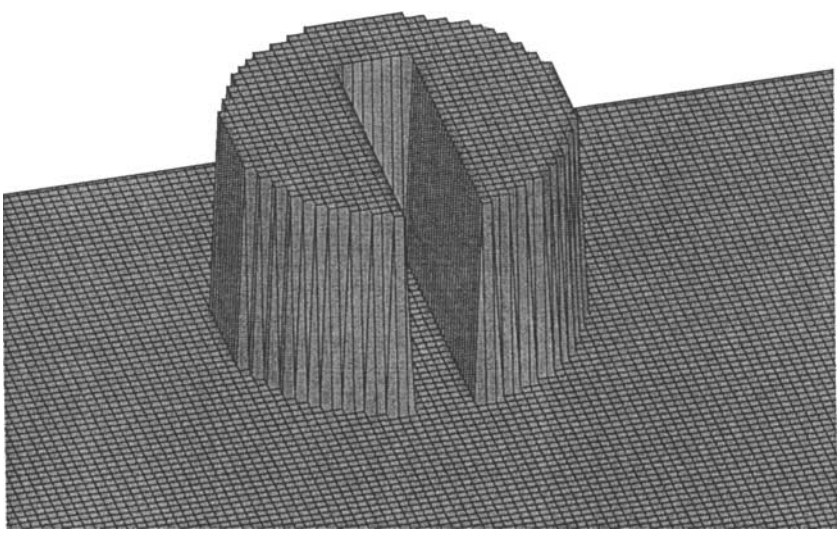

FIG. 5. Perspective view of the initial profile for the rotation of a cut-out cylinder.

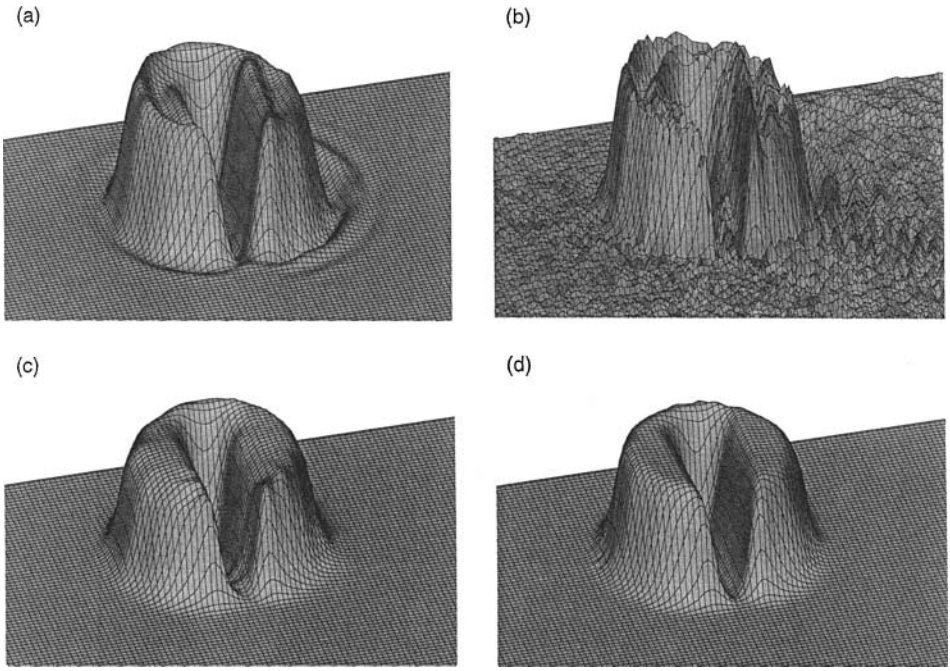

FIG. 6. Perspective view of the numerical results for the rotation of a cut-out cylinder after one full cycle: (a) fifth-order upwind-biased scheme; (b) Pade scheme; (c) ENO-Roe scheme; (d) ENO-Pade scheme.

The computational domain is $x \in [-5, 5]$ in this case. Numerical results of the density profile for different schemes at $t = 1.8$ with 200 and 400 grid points are shown in Figs. 8 and 9, respectively. A constant time-step size of $\Delta t = 0.005$ is used for the mesh with 200 points and $\Delta t = 0.0025$ is applied for the finer mesh.

In the figures, the solid line is the numerical solution of an ENO-Padé scheme with 1600 nodal points; this can be regarded as the grid-independent solution. This ENO-Padé

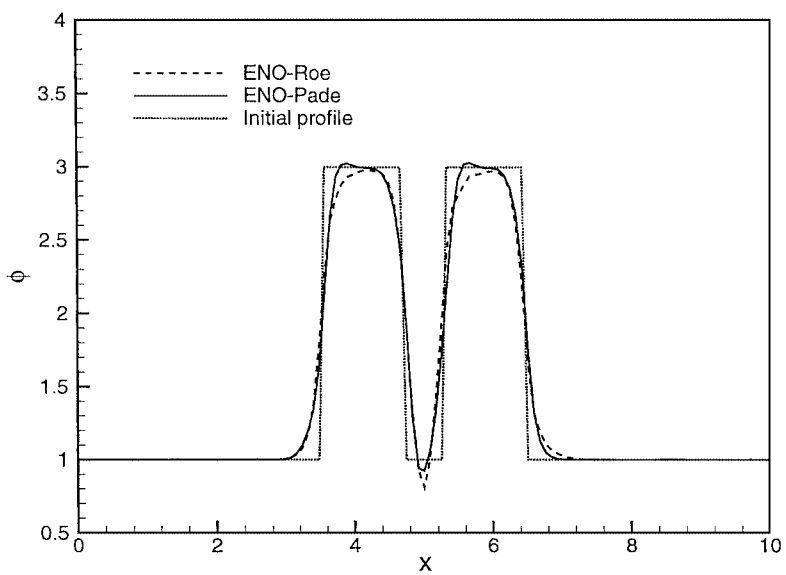

FIG. 7. Comparison of the predicted profiles (along $y = 7.5$) by ENO-Roe and ENO-Pade schemes.

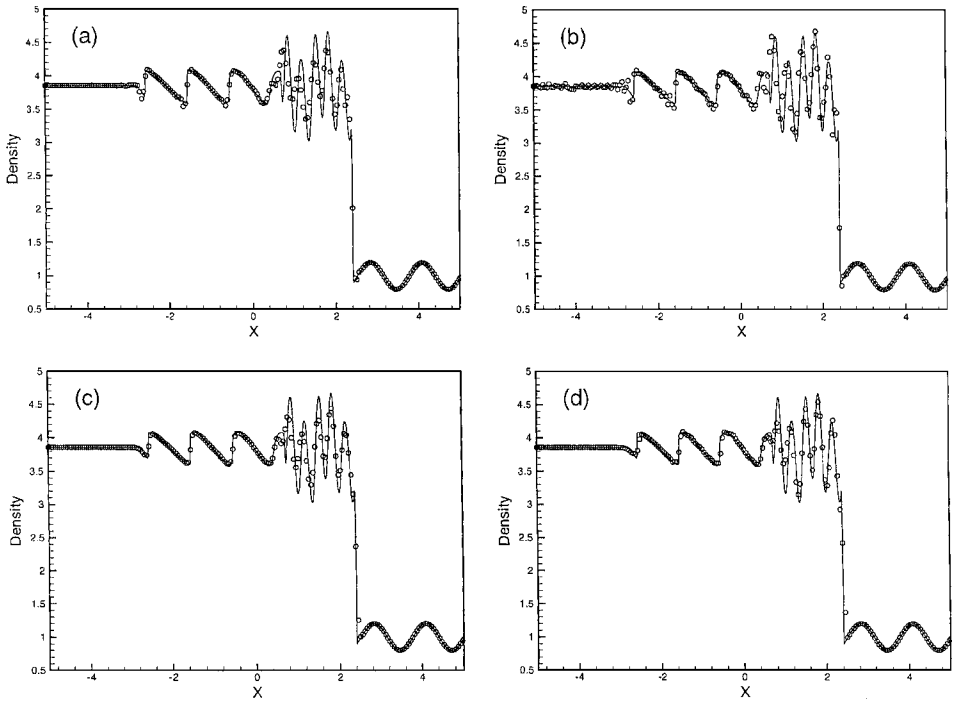

FIG. 8. Numerical results of shock/disturbance interaction problem with 200 nodal points at $t = 1.8$: (a) fifth-order upwind-biased scheme; (b) Pade scheme; (c) ENO-Roe scheme; (d) ENO-Pade scheme. (Solid line is regarded as the grid-independent solution.)

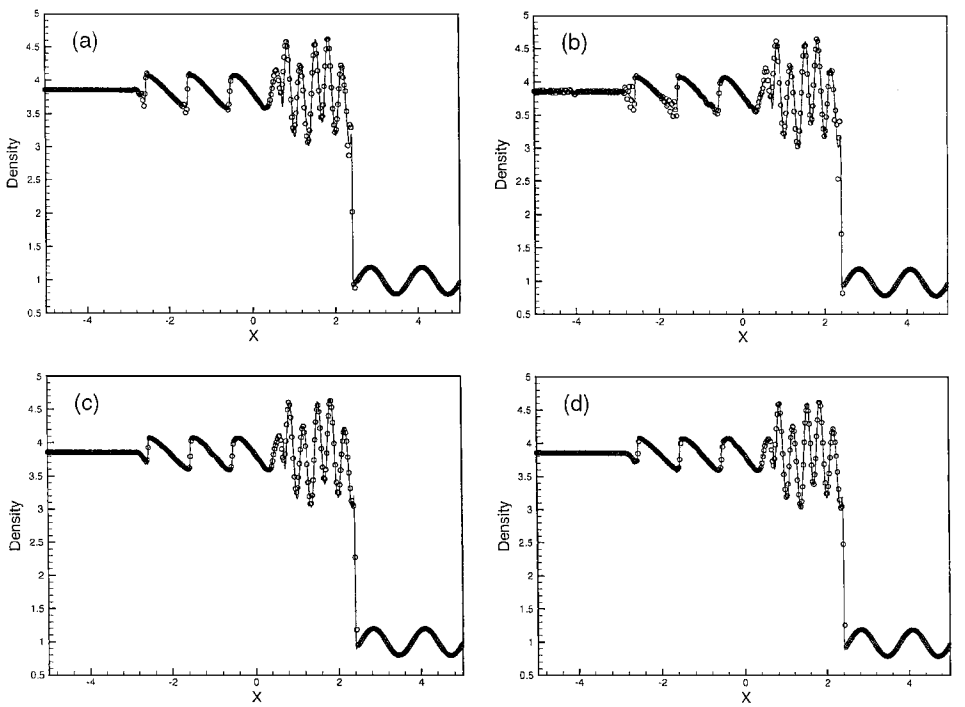

FIG. 9. Numerical results of shock/disturbance interaction problem with 400 nodal points at $t = 1.8$: (a) fifth-order upwind-biased scheme; (b) Pade scheme; (c) ENO-Roe scheme; (d) ENO-Pade scheme. (Solid line is regarded as the grid-independent solution.)

solution is compared to the numerical results with the same resolution in [7, 14, 19] and they are virtually identical. From these figures, it can be seen that both the ENO-Roe scheme and the ENO-Padé scheme exhibit excellent performance in capturing the moving shock and the fine structures in the postshock regions. Their solutions with 400 grid points (Figs. 9c and 9d) almost match the grid-independent solution.

The next test case is the inviscid, unsteady advection of a vortex in a uniform flow. This problem can be used to test the capability of a numerical scheme to accurately advect the vortex structures, a capability that is essential and critical in LES/DNS of turbulent flows.

The initial flow field is given by imposing a vortex on a uniform flow with a free-stream Mach number $M_\infty = 0.1$. The initial conditions of this case can be prescribed by the relations [15]

$$u = U_\infty - \frac{C(y - y_c)}{R^2} \exp(-r^2/2), \tag{28a}$$

$$v = \frac{C(x - x_c)}{R^2} \exp(-r^2/2), \tag{28b}$$

$$p - p_\infty = -\frac{\rho C^2}{2R^2} \exp(-r^2), \tag{28c}$$

with

$$r^2 = \frac{(x - x_c)^2 + (y - y_c)^2}{R^2},$$

where $(x_c, y_c) = (0, 0)$ is the center of the initial vortex, R is the radius of the vortex core, and C is the circulation. The computational domain is set to $x/R \in [-6, 18]$, $y/R \in [-6, 6]$ and the dimensionless vortex strength, $C/(U_\infty R)$, is taken to be 0.02 in our computation.

The 2-D Euler equations with the above initial conditions are solved with a uniform mesh of 60×30 nodes, and a nondimensional time-step size of $(\Delta t U_\infty)/R = 0.04$, which corresponds to a CFL number of 0.1, is applied in this case.

Figure 10 shows the comparison of the vorticity magnitude contours at three different nondimensional time levels, $T = 0$, 6, and 12. It is clear that the fifth-order upwind-biased scheme shows strong dissipation during the advection and that the ENO-Roe scheme also exhibits some degrees of dissipation. Both the Padé scheme and the ENO-Padé scheme exhibit nondissipative behavior and the predicted vortices remain almost unchanged during the advection.

Figure 11 shows the swirl velocities of the vortex along the $y/R = 0$ line at $T = 12$. The results of the Padé, ENO-Roe, and ENO-Padé schemes agree closely with the exact solution, while large dissipative errors can be clearly seen for the fifth-order upwind-biased scheme.

The last test case in this paper is a steady-state inviscid oblique shock reflection problem. This test case was used in [25] to test the performances of shock-capturing schemes. The problem involves the reflection of an oblique shock produced at the inlet section of a plane inviscid channel flow with a Mach number of 2.9. The Rankine–Hugoniot oblique shock relationships are used to impose the boundary conditions on the top surface of

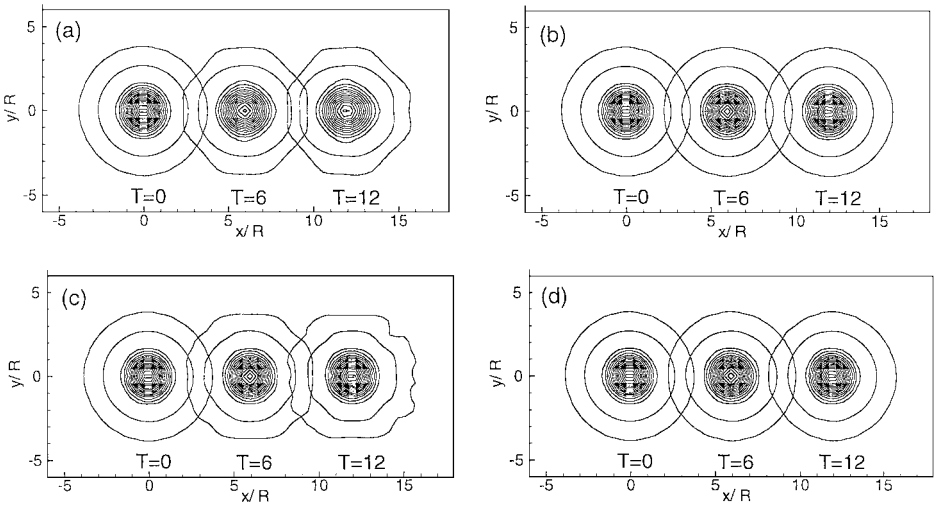

FIG. 10. Vorticity magnitude contours at three different nondimensional time levels: (a) fifth-order upwind-biased scheme; (b) Pade scheme; (c) ENO-Roe scheme; (d) ENO-Pade scheme.

the domain such that a 29 degree oblique shock is created. The bottom surface of the domain is an insulated slip wall and the outflow boundary conditions are applied at the outlet.

The computational domain is $x \in [0, 4.1]$, $y \in [0, 1]$ and the numerical simulations with different schemes are performed on a uniform mesh of 80×30. A comparison of the predicted pressure contours is shown in Fig. 12. Again, the fifth-order upwind-biased scheme and the Padé scheme display severe spurious oscillations near the shocks, while both the ENO-Roe and the ENO-Padé schemes show essentially nonoscillatory behavior across the shocks.

In order to justify the shock-capturing ability of the ENO-Roe scheme and the ENO-Padé scheme, the computations are repeated for these two schemes on a very coarse mesh of 40×20 nodes. The comparison of the pressure coefficients along the $y = 0.5$ line is shown in Fig. 13. From this figure, it can be seen that the ENO-Padé scheme presents a slightly better performance than the ENO-Roe scheme does in this case.

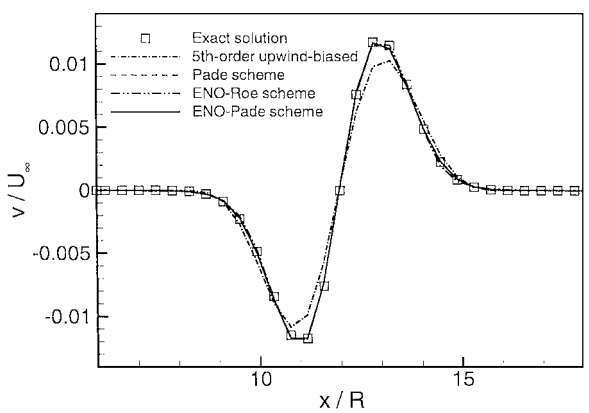

FIG. 11. Comparison of the swirl velocities at $T = 12$ along the $y/R = 0$ line.

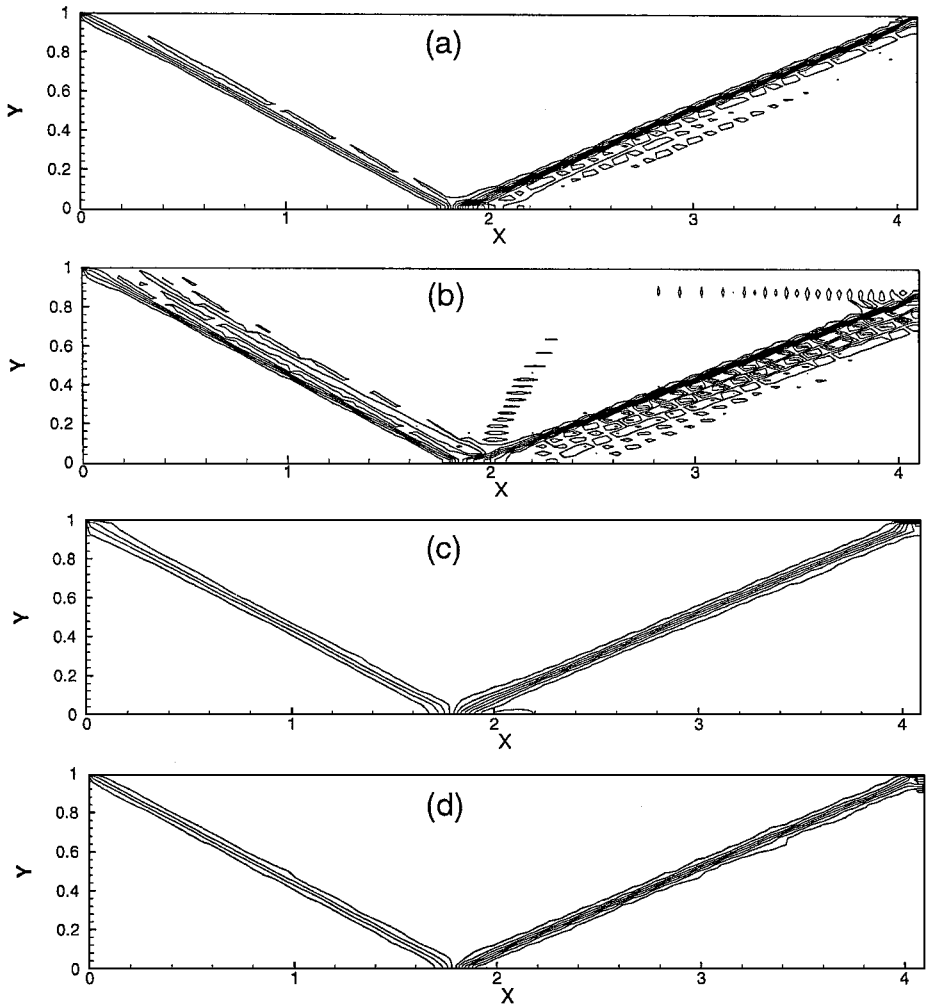

FIG. 12. Comparison of the pressure contours for a 2-D inviscid oblique shock-reflection problem: (a) fifth-order upwind-biased scheme; (b) Pade scheme; (c) ENO-Roe scheme; (d) ENO-Pade scheme.

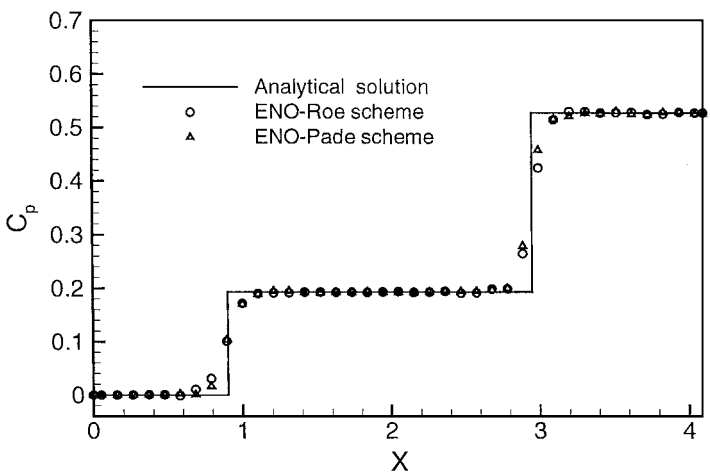

FIG. 13. Comparison of the pressure coefficients along the $y = 0.5$ line with a mesh of 40×20.

5. CONCLUDING REMARKS

A new methodology to construct an essentially nonoscillatory, high-order Padé-type (ENO-Padé) scheme has been developed and tested in this paper. The proposed ENO-Padé scheme can be considered as a blend of the Padé scheme and ENO ideas. The use of the adaptive stencils in the ENO interpolation procedure can eliminate or at least suppress the nonphysical oscillation and the nonlinear instability arising in the computation, while the use of the Padé formula can improve the numerical accuracy in smooth regions. The ENO-Padé scheme has been validated in a number of numerical test cases, including two scalar convection problems and three compressible flows, and it exhibits excellent performances in all test cases.

APPENDIX: GLOBAL CONSERVATION APPROACH FOR NEAR-BOUNDARY SCHEMES

As presented in Section 2, the cell-centered Padé scheme (2) is applied at all interior points ($i = 3, \ldots, N-2$), and two one-sided boundary schemes, (4) and (5), are used for $i = 1$ and $i = N$, respectively. Now, suppose the same Padé scheme (2), but not necessarily with the same coefficients, is used for near-boundary points $i = 2$ and $i = N-1$; then we can write the overall schemes in a matrix form as

$$\mathbf{A}\mathbf{f}' = \frac{1}{h}\mathbf{B}\hat{\mathbf{f}}, \tag{A.1}$$

where $\mathbf{A}$ is an $N \times N$ sparse matrix and $\mathbf{B}$ is an $N \times (N+1)$ sparse matrix. $\mathbf{f}', \hat{\mathbf{f}}$ are the corresponding $N, N+1$ vectors, respectively. $\mathbf{f}'$ represents the first derivatives at all nodal points ($i = 1, 2, \ldots, N$) and $\hat{\mathbf{f}}$ stands for the field values at all cell interfaces ($i = \frac{1}{2}, \frac{3}{2}, \ldots, N+\frac{1}{2}$). To satisfy the global conservation constraint, it is sufficient to require that columns 2 through N of matrix $\mathbf{B}$ sum exactly to zero. This ensures that only the field values at the boundary cell-edges contribute to the boundary fluxes and hence guarantee the global conservation.

Substituting the Padé scheme (2) and the boundary schemes (4) and (5) into the above matrix form (A.1), we have

$$\mathbf{A} = \begin{pmatrix} w_1 & w_1\alpha_1 & 0 & 0 & 0 & 0 & \ldots & 0 \\ w_2\hat{\alpha} & w_2 & w_2\hat{\alpha} & 0 & 0 & 0 & \ldots & 0 \\ 0 & \alpha & 1 & \alpha & 0 & 0 & \ldots & 0 \\ 0 & 0 & \alpha & 1 & \alpha & 0 & \ldots & 0 \\ 0 & 0 & 0 & \alpha & 1 & \alpha & \ldots & 0 \\ \vdots & \vdots & \vdots & \vdots & \vdots & \vdots & \ddots & \vdots \end{pmatrix}, \tag{A.2}$$

$$\mathbf{B} = \begin{pmatrix} w_1a_1 & w_1b_1 & w_1c_1 & 0 & 0 & 0 & 0 & \ldots & 0 \\ -w_2\hat{b} & -w_2\hat{a} & w_2\hat{a} & w_2\hat{b} & 0 & 0 & 0 & \ldots & 0 \\ 0 & -b & -a & a & b & 0 & 0 & \ldots & 0 \\ 0 & 0 & -b & -a & a & b & 0 & \ldots & 0 \\ 0 & 0 & 0 & -b & -a & a & b & \ldots & 0 \\ \vdots & \vdots & \vdots & \vdots & \vdots & \vdots & \vdots & \ddots & \vdots \end{pmatrix}. \tag{A.3}$$

Here, it is sufficient to consider only the entries in the top left corner of **A** and **B**. The other corner can be treated in the same way. Two explicit weights, w_1 and w_2, are also introduced at near-boundary points and $\hat{\alpha}$, $\hat{a}$, $\hat{b}$ are the coefficients to be determined through the global conservation restriction.

Setting the sum of column 2, column 3, and column 4 of matrix **B** to exactly zero, the following equation can be derived:

$$\frac{\hat{a}}{\hat{b}} = \frac{b_1}{b_1 + c_1}\frac{a}{b} + \frac{b_1 - c_1}{b_1 + c_1}. \tag{A.4}$$

The only unknowns in Eq. (A.4) are $\hat{a}$ and $\hat{b}$, while a, b, b_1, c_1, are the known coefficients. Also, two additional formulae relating $\hat{a}$ and $\hat{b}$ with $\hat{\alpha}$ can be derived through a Taylor series analysis, i.e.,

$$\hat{a} = \frac{9 - 6\hat{\alpha}}{8}, \tag{A.5}$$

$$\hat{b} = \frac{-1 + 22\hat{\alpha}}{8}. \tag{A.6}$$

The truncation error of the above scheme is $\frac{9-62\hat{\alpha}}{1920}h^4(\partial^5 f/\partial x^5)$. This scheme is normally fourth-order accurate. With $\hat{\alpha} = 9/62$, the scheme reverts to exactly the one used for the interior points and it is sixth-order accurate.

Solving the combined equations of (A.4), (A.5), and (A.6), we can get the coefficients of the near-boundary scheme which satisfies the global conservation requirement in a discrete analog,

$$\hat{\alpha} = \frac{55}{666}, \quad \hat{a} = \frac{118}{111}, \quad \hat{b} = \frac{34}{333}. \tag{A.7}$$

ACKNOWLEDGMENTS

The work of the first author was supported by the Center for Computational Sciences, University of Kentucky, and the work of the second author was supported in part by the NASA Glenn Research Center under Grant NAG3-2099 and by a Kentucky NASA EPSCoR Grant.

REFERENCES

1. S. K. Lele, Compact finite difference schemes with spectral-like resolution, *J. Comput. Phys.* **103**, 16 (1992).
2. A. G. Kravchenko, P. Moin, and K. Shariff, *B-Spline Method and Zonal Grids for Simulations of Complex Turbulent Flows*, AIAA Paper 97-0433, 35th AIAA Aerospace Sciences Meeting and Exhibit, Reno, NV (1997).
3. A. G. Kravchenko and P. Moin, *B-Spline Methods and Zonal Grids for Numerical Simulations of Turbulent Flows*, Report No. TF-73 (Department of Mechanical Engineering, Stanford University, 1998).
4. S. T. Zalesak, Fully multidimensional flux-corrected transport algorithms for fluids, *J. Comput. Phys.* **31**, 335 (1979).
5. A. Harten, B. Engquist, S. Osher, and S. Chakravarthy, Uniformly high order essentially non-oscillatory schemes III, *J. Comput. Phys.* **71**, 231 (1987).
6. C.-W. Shu and S. Osher, Efficient implementation of essentially non-oscillatory shock-capturing schemes, *J. Comput. Phys.* **77**, 439 (1988).

7. C.-W. Shu and S. Osher, Efficient implementation of essentially non-oscillatory shock-capturing schemes, II, *J. Comput. Phys.* **83**, 32 (1989).
8. C.-W. Shu, *Essentially Non-Oscillatory and Weighted Essentially Non-Oscillatory Schemes for Hyperbolic Conservation Laws*, NASA/CR-97-206253 (1997).
9. X.-D. Liu, S. Osher, and T. Chan, Weighted essentially nonoscillatory schemes, *J. Comput. Phys.* **115**, 200 (1994).
10. G. Jiang and C.-W. Shu, Efficient implementation of weighted ENO schemes, *J. Comput. Phys.* **126**, 202 (1996).
11. M. M. Rai and P. Moin, Direct simulations of turbulent flow using finite-difference schemes, *J. Comput. Phys.* **96**, 15 (1991).
12. P. G. Huang, *Computation of turbulent flows using upwind-biased 5th-order schemes*, Proceeding of the Eleventh Symposium on Turbulent Shear Flows, Vol. 2, 2–83, (Grenoble, France, September 8–10, 1997).
13. K. Mahesh, P. Moin, and S. K. Lele, *The Interaction of a Shock Wave with a Turbulent Shear Flow*, Report No. TF-69 (Department of Mechanical Engineering, Stanford University, 1997).
14. X. Deng and H. Maekawa, Compact high-order accurate nonlinear schemes, *J. Comput. Phys.* **130**, 77 (1997).
15. M. R. Visbal and D. V. Gaitonde, *High-Order Accurate Methods for Unsteady Vortical Flows on Curvilinear Meshes*, AIAA Paper 98-0131, 36th AIAA Aerospace Sciences Meeting and Exhibit, Reno, NV (1998).
16. D. V. Gaitonde and M. R. Visbal, *Further Development of a Navier–Stokes Solution Procedure Based on Higher-Order Formulas*, AIAA Paper 99-0557, 37th AIAA Aerospace Sciences Meeting and Exhibit, Reno, NV (1999).
17. B. Cockburn and C.-W. Shu, Nonlinearly stable compact schemes for shock calculations, *SIAM J. Numer. Anal.* **31**, 607 (1994).
18. H. C. Yee, Explicit and implicit multidimensional compact high-resolution shock-capturing methods: Formulation, *J. Comput. Phys.* **131**, 216 (1997).
19. N. A. Adams and K. Shariff, A high-resolution hybrid compact-ENO scheme for shock-turbulence interaction problems, *J. Comput. Phys.* **127**, 27 (1996).
20. E. Fatemi, J. Jerome, and S. Osher, Solution of the hydrodynamic device model using high order non-oscillatory shock capturing algorithms, *IEEE Trans. Comput. Aided Design Integrated Circuits Syst.* **10**, 232 (1991).
21. C.-W. Shu, Numerical experiments on the accuracy of ENO and modified ENO schemes, *J. Sci. Comput.* **5**, 127 (1990).
22. P. L. Roe, Approximate Riemann solvers, parameter vectors and difference schemes, *J. Comput. Phys.* **43**, 357 (1981).
23. A. M. Rogerson and E. Meiburg, A numerical study of the convergence properties of ENO schemes, *J. Sci. Comput.* **5**, 151 (1990).
24. J. F. McKenzie and K. O. Westphal, *Phys. Fluids* **11**, 2350 (1968).
25. H. C. Yee, *Upwind and Symmetric Shock Capturing Schemes*, NASA TM 89464 (1987).